# Redox induced sulfur-selenium isotope decoupling recorded in pyrite

S. König[1], B. Eickmann[1], T. Zack[2], A. Yierpan[1], Wille M.[3], H. Taubald[1], R. Schoenberg[1]

[1]Isotope Geochemistry, Department of Geosciences, University of Tübingen, Germany

[2]Department of Earth Sciences, University of Gothenburg, Sweden

[3]Department of Geochemistry, Institute of Geological Sciences, University of Bern, Switzerland

## ABSTRACT

This study is the first combined S and Se isotope investigation of sulfide suited to explore differences in fractionation between these two redox sensitive isotope systematics as recorded in the same mineral. A first case study of cretacious Navajún pyrite from the mesozoic Cameros Basin, Spain, with known petrogenesis and geological context shows systematic decoupling at the microscale: Variable S isotope values within the analyzed pyrite coincide with rather constant Se isotope values and vice versa. These signatures were not generated during pyrite growth but record previous redox induced fractionations in fluids that each contributed both elements from two sources. It is likely that both S and Se isotope fractionation occurred during strong reduction from one fully oxidized source whereas only S but no Se isotope fractionation occurred during minor reduction following sulfide dissolution via $H_2O$ from another source. Subsequent mixing of these two $H_2S$-$H_2Se$ fluids at different elemental S-Se ratios during pyrite incorporation can then explain the S-Se isotope variations in the investigated specimen. These inferences are in accordance with a larger range in the redox potential Eh of Se relative to S, resulting in coupled or decoupled Se and S isotope fractionation depending on the oxygen fugacity $fO_2$ during the reduction process. If extended to other sulfides of diverse origin, for a given pH, combined Se and S isotope studies may allow to investigate the magnitude of redox variations and place more robust constraints on

minimum and maximum oxygen concentrations in the source. We therefore suggest combined S-Se isotope analyses in sulfide as a new powerful proxy for studying Earth's redox evolution beyond the bulk rock scale.

## 1. INTRODUCTION

The development of Earth into a habitable Planet is linked to its redox evolution and the dynamic variability of atmospheric volatiles. Geochemical proxies are frequently used tools to study the rock and mineral record of this redox history. The Se isotope system has recently received increased interest as a valuable, novel palaeo-redox proxy (see review by Stüeken, 2017). Within this scope, detailed studies focusing on combined S-Se isotope systematics at the mineral scale, in addition to bulk sediments, may help to adequately interpret the growing Se isotope database of the geological rock record and its potential to investigate the terrestrial redox evolution.

Selenium can occur in VI, IV, 0, and -II valences. Redox reactions affecting Se are both biotic (e.g., microbially controlled; Oremland, 1994; White and Dubrovsky, 1994) and abiotic (e.g., Johnson, 2004). Under surface conditions Se(VI) and Se(IV) oxyanions are soluble, whereas elemental Se(0) is insoluble. Hence, the reduction of Se may reduce its mobility and bioavailability in the solution. Selenium has six stable isotopes: $^{74}$Se, $^{76}$Se, $^{77}$Se, $^{78}$Se, $^{80}$Se, and $^{82}$Se, with relative abundances of ca. 0.9%, 9.4%, 7.6%, 23.8%, 49.6% and 8.7%, respectively (Johnson and Bullen, 2003). Oxidized Se compounds tend to be isotopically heavier than reduced Se compounds (e.g., Johnson, 2004). As such, Se isotopes were recognized as sensitive tracers of redox and biogeochemical transformations (e.g., Krouse and Thode, 1962; Johnson et al., 1999; Herbel et al., 2000; Rouxel et al., 2002; Ellis et al., 2003; Clark and Johnson, 2010; Schilling et al. 2011) and abiotic transportation/mobilization of Se (Johnson and Bullen, 2003; Mitchell et al. 2013; Zhu et al., 2014). Selenium isotope systematics have already been applied to investigate the terrestrial paleo-redox record (Mitchell et al., 2012, 2016; Stüeken et al., 2015a, b; Pogge Von Strandmann et al.,

2014; 2015; Kipp et al., 2017) and formation of modern and ancient seafloor hydrothermal environments (Rouxel et al., 2004; Layton-Matthews al., 2013). Moreover, the smaller stability of sulfide relative to selenide make the Se isotope system less sensitive to subtle redox changes at lower Eh but more sensitive to rdox changes at higher Eh, relative to the S isotope system (e.g., Johnson, 2014).

In addition to Se isotopes, Se/Te concentration ratios in chemical marine mineral phases have been noted as a potential palaeo-redox proxy indicative for the presence of Mn-oxides (Schirmer et al., 2014), due to the large Te enrichments from seawater in Mn-oxides relative to Se (Hein et al., 2003). Thus, in combination with existing analytical protocols for S isotope analysis, the combined investigation of the same rocks and potentially minerals using the three redox proxies S-Se isotopes and S-Se-Te ratios may lead to improved constraints of the redox evolution in the geological record. Moreover, as the triplet S-Se-Te is chalcophile it is enriched in similar geological materials such as sulfides and sulfide-rich sediments. However, S and Se isotopes in sulfides and sediments have not yet been systematically combined. Neither have any of these isotope systems ever been systematically coupled to Se and Te elemental investigations. Such comparative studies are now possible due to recent analytical progress regarding chemical sample processing and instrumental techniques for combined determination of sub ng $g^{-1}$ Se and Te as well as precise Se isotope ratios on as low as 5 ng total Se (Kurzawa et al., 2017; Yierpan et al., 2018).

In this study we combine the new Se and Te analytical techniques with S isotope analysis to allow for microscale application of three redox proxies: S and Se isotopes as well as S-Se-Te element concentrations of the same pyrite material. We focus on a pyrite from Navajún, Spain, for which genesis, environment and abiotic redox-related S isotope systematics are already constrained. This provides a suitable background to interpret our new S-Se isotope data and evaluate the potential of combined S-Se isotopes for future investigation of Earth's redox signature at the mineral- and microscale. Especially the possibility to distinguish between individual pyrites may help to understand the sum of their signatures in bulk sediments.

## 2. SAMPLE MATERIAL: THE NAVAJÚN PYRITES

A Navajún pyrite specimen from the mesozoic Cameros Basin in NE Spain has been especially selected for this study for the following reasons: i) The locality is worldwide famous for size and number of pyrite crystals that are available to scientists and collectors alike and specimens are sufficiently large to yield abundant material for investigations. Particularly the large crystal size enables the investigation of Se and Te concentration heterogeneities within the pyrite matrix by comparison of LA-ICP-MS and solution ICP-MS. ii) Genesis of the pyrites is well constrained and provides a reliable background for studying Se isotope systematics. iii) Sulfur isotope data are published for other pyrite specimens from the same locality (Alonso-Azcárate et al., 1999a; 2001) and a model has been developed for the S isotope variations within these sulfides. This enables a comparison to our new S isotope data and provides a framework for evaluating combined Se-S isotope systematics. iv) High temperatures ensure that S and Se are affected by abiotic redox processes only after their release from their sources and allow a focused discussion without the necessity to consider biological processes. v) It has been shown that different specimens within the Navajún suite and even the entire Cameros Basin all share genetic similarities. Although in different extents, geochemical and S isotope variations within one specimen are therefore often representative of the processes involved in pyrite systematics of the entire area. This provides the possibility to assess the role of these processes on combined S-Se isotope systematics from a representative specimen alone.

The Navajún pyrites are hosted by the Mesozoic metasediments of the Cameros Basin, NW Spain (Fig. 1a). Well-defined pyrite cubes represent the most common habit in most deposits in the Cameros Basin and a 3 $cm^3$ pyrite cube was therefore chosen for this study (Fig. 1b). A high density of inclusions has been previously noted (Alonso-Azcárate, 1999a). Several types of inclusions have

104 been described such as phyllosilicates (illite and chlorite), quartz, chloritoid chalcopyrite, sphalerite,
105 iron oxides and occasionally inclusions of calcite, dolomite and anhydrite.

106 Pyrite growth is locally associated to fractures in the mineralized pelites. These fractures are
107 early, syn-depositional structures thought to have formed during deposition, diagenesis and
108 compaction of the sediments. Introduction of locally derived sulfidic metamorphic fluids occurs
109 through permeable sandstone layers and concentrates along the local fractures, ultimately reaching
110 Fe-rich chlorite-bearing pelite beds (Alonso-Azcárate et al., 1999a). Sulfidation of Fe-Mg silicates
111 in the metapelites leads to local remobilization of iron that forms the pyrite deposit. Iron is available
112 more or less directly at the site of pyrite formation. Low S content in the metapelite itself indicates
113 that reduced sulfur, however, is supplied from two distinct sources with transport distances in the
114 range of hundreds of meters within the basin (Alonso-Azcárate, 1999a). One S source is attributed
115 to thermochemical sulfate reduction (TSR) and another to metamorphic dissolution of sedimentary
116 sulfide (sulfide dissolution, SD). Moreover, geothermometric calculations using chlorite chemistry
117 yield a temperature of ca. 370°C during pyrite growth (Alonso-Azcárarate et al., 1999b), consistent
118 with the maximum temperature estimated for metamorphism in the Cameros Basin (Casquet et al.,
119 1992).

120 Variable mixing of $H_2S$ from these two SD and TSR sources leads to the full range of S
121 isotope compositions in all pyrite deposits of the Cameros Basin with $\delta^{34}S$ values from -10 ‰ to
122 +14 ‰ (Alonso-Azcárarate et al., 1999a). This is supported by the fact that, rather minor
123 differences in temperature and fluid chemistry occur across the same sedimentary basin that could
124 only account for much smaller variations in S isotopic composition (Ohmoto and Rye, 1979) than
125 observed among all pyrites of the area. Each individual deposit has a much more limited range in S
126 isotope composition and two main Navajún pyrite subgroups were identified in distinct sandstone
127 units with average $\delta^{34}S$ values of -2.4 ‰ (type A) and +10 ‰ (type B), respectively. Absence of
128 zoning-dependent S isotopic variation indicates a lack of systematic isotopic fractionation related to
129 crystal growth (Alonso-Azcárate, 1999a). Therefore the S isotope signature of each individual

130 pyrite can be used to trace back the original S isotope signature of the SD-TSR mixture. The SD of
131 sedimentary pyrite in the basin to form pyrrhotite in the presence of organic carbon and a fluid very
132 rich in $H_2S$ (Ferry, 1981; Oliver et al., 1992) triggered a kinetic isotopic effect that produced
133 pyrrhotite with high $\delta^{34}S$ values and $H_2S$ with low $\delta^{34}S$ values (Kajiwara et al., 1981; Yamamoto,
134 1984). The SD related kinetic S isotopic fractionation is then likely following only minor redox
135 variation. On the other hand a large redox variation is linked to the TSR of abundant gypsum units
136 in the area with $\delta^{34}S$ = +12 ‰ (Alonso-Azcárate, 1999a), but temperatures of ca. 220°C are
137 believed to have prevented strong S isotopic fractionation (Krouse, 1977; Machel et al., 1995). The
138 $H_2S$ produced by TSR therefore provide a source of high $\delta^{34}S$ values. These constraints on pyrite
139 genesis and SD vs. TSR-dependent abiotic fractionations of S isotope and isotope mixing are the
140 background to study our new Se isotopes and interpret combined S-Se isotope systematics within
141 the Navajún pyrite.
142
143 3. ANALYTICAL TECHNIQUES
144
145 3.1 Sample processing
146
147 For LA-ICP-MS analyses (Table in Electronic Appendix), a thick section from nearly the entire
148 width (ca. 3 cm) of one side of the pyrite crystal was prepared (Fig. 1b). To place the small scale Se
149 and Te concentration heterogeneity identified by this in-situ analysis into context of the solution
150 ICP-MS data, three sample processing strategies for wet chemical analysis were explored that are
151 herein referred to as i) representative powder (RP), ii) unrepresentative powder (UP) and iii)
152 individual microsamples (SPL). Se isotopes were analyzed from powdered fractions of i), ii) and
153 iii), whereas S isotopes were only analyzed on a subset of material from i) and iii). All data are
154 summarized in Table 1.
155

i) In a first step, we aimed to prepare homogeneous powder that can be regarded as representative of the bulk pyrite (RP-1 to 11). This powder was used to constrain the overall reproducibility of the analytical method as well as the bulk pyrite S- isotope (RP-1 to 3), Se isotope and elemental S-Se-Te concentrations. In order to obtain a bulk representative powder, a total of 30 g pyrite material was removed from different sides and within the original cube crystal with a steel saw and ground with an agate mortar to coarse powder. The powder was further fine-ground to a grain size < 25 µm using a Planetary mill *(PULVERISETTE 7©, Fritsch*). From this material homogenized powders of 5 to 50 mg, amounting to Se masses between 25 to 250 ng, were used for digestion.

ii) Potential heterogeneity effects by unrepresentative sample processing, despite weighing relatively large amounts of powder were explored. For this, 2 pieces amounting to less than 1 g of pyrite material were cut from different sides of the pyrite cube and separately ground to powder with an agate mortar. Each of the two powdered pieces were used for 2 digestions of 50 mg powder, respectively (UP-1a,b and UP-2a,b).

iii) Individual pyrite microsamples (SPL-1 to 10) ranging in size between 3 to 13 mg were cut from different sides and within the cubic crystal to sample areas from rim to halfway into the specimen. Microsamples were separately powdered and, after 0.1 mg aliquot removed from each powdered microsample for S isotope analyses (SPL-1 to 7), each powdered microsample was individually digested. This was done in order to investigate if potential S-Se-Te elemental heterogeneity effects within the pyrite (between single microsamples) are systematically related to S-Se isotope variations. We preferred this approach rather than a microdrill extraction as no zoning-dependent S isotope variations were previously detected and microdrill extraction generates mixed powders for core drills, potentially obscuring correlations between concentrations and isotope variations. Digestion of individual pyrite microsamples of as little as 3 mg also pushes the boundary for S-Se isotope investigation to the microscale.

182

183 3.2 Reagents and materials

184

185 Commercially available reagent grade HF, HCl and $HNO_3$ were further distilled in a DST-
186 1000 acid purification system (Savillex). Analytical grade $NaBH_4$ and NaOH were used to prepare
187 the reduction agent for hydride generator. The standard solutions include NIST SRM 3149 and MH
188 495 (15 and 30 ng $mL^{-1}$) for Se isotope analysis and NIST SRM 3156 (0.5 ng $mL^{-1}$) for Te
189 elemental analysis. A calibrated Se double spike (Kurzawa et al., 2017) and Te single spike (~92%
190 $^{125}Te$) were used.

191 All the Savillex beakers were cleaned by successive leaching in reagent grade HCl, $HNO_3$
192 and 18.2 MΩ·cm $H_2O$ (Milli-Q purification system) at 120 °C for two days. For the chemical
193 purification method pre-cleaned polypropylene columns (Spectra/Chrom®) were filled with 3 mL
194 Eichrom AG1-X8 (100-200 mesh) anion exchange resin. A fresh resin was used for each
195 purification procedure.

196

197 3.3 Chemistry

198

199 Purification of the Te spike was required in order to eliminate trace amounts of Se that
200 would otherwise interfere with Se stable isotope measurements. For this, 10 g of a 10 µg $g^{-1}$ $^{125}Te$
201 spike (König et al., 2012; 2015) was weighed into a Savillex beaker, dried down at 85°C, re-
202 dissolved in 5 mL 4 M HCl. Seven ml of anion exchange resin was placed into a polypropylene
203 column (8 cm bed height, Triskem) and cleaned alternately with 5 mL of 18.2 MΩ·cm water and 1
204 M $HNO_3$ twice. Following 2 x 5 mL water addition, the resin was conditioned with 2 x 5 mL 4 M
205 HCl. The $^{125}Te$ spike solution was then loaded onto the column. Selenium was quantitatively
206 separated by adding 9 mL 4 M HCl and Te was eluted in 14 mL 0.4 M HCl (Yierpan et al., 2018).
207 The Te cut was subsequently evaporated to complete dryness at 85 °C and the column separation

208 procedure was repeated twice to ensure complete Se removal. The final $^{125}$Te spike, now containing
209 only background-level Se, was diluted to the desired concentrations (~63 ng ng$^{-1}$) and kept in 5%
210 $HNO_3$. The Te recovery after the three purification procedures is >95%.

211 For digestion of the pyrites, samples and spike solutions were weighed into 15 mL Savillex
212 beakers, 1 ml 10.5 M HCl and 1 ml 14.5 M $HNO_3$ were added and closed beakers were placed on a
213 hotplate at 85°C for 24 h. Following complete evaporation at 65°C, the samples were taken up in 2
214 mL 6 M HCl and placed on a hotplate at 85°C for 12 h and dried down again. Samples were re-
215 dissolved in 3 mL 6 M HCl and purified for Se and Te following the method of Yierpan et al.
216 (2018) with minor modifications. Briefly, the 3 mL resin was cleaned with $H_2O$ and conditioned
217 with 6 M HCl. The sample was then loaded onto the columns and eluted with 9 mL 6 M HCl to
218 collect Se. After separating Fe with 8 mL 2 M HCl–5 M HF mixture and 4 mL 0.4 M HCl, Te was
219 eluted in 14 mL 0.4 M HCl. Finally, the pure Se and Te fractions (ca. 80% recoveries by isotope
220 dilution) were both dried down at 85°C, dissolved in 1 mL 2 M HCl, aliquoted and diluted for
221 analyses. Unlike Se purification in a complex matrix such as basalts, the Se cut was not further
222 purified via a cation exchange resin. This is because the hydride generator serves to isolate any
223 remaining matrices from Se and the observed $H_2Se$ formation efficiency was always quantitative
224 after the Fe separation. Therefore, 6 M HCl was used instead of 4 M HCl in order to completely
225 isolate Fe from Se via one-step column chemistry only (Wang and Becker, 2014) although a higher
226 Se recovery can be obtained at lower molarity (Yierpan et al., 2018; and references therein).
227
228 3.4 Selenium isotope measurements
229
230 Following chemical separation stable Se isotope ratios were analyzed on a ThermoFisher Scientific
231 NeptunePlus MC-ICP-MS linked with a CETAC HGX-200 hydride generator at the University of
232 Tübingen, Germany, following the analytical procedure described in detail by Kurzawa et al.
233 (2017). Digested and purified samples were further diluted and generally ca. 15-30 ng of sample Se

was used, which typically generated 550-1100 mV on $^{82}Se$ with a $10^{11}$ Ω amplifier resistor under typical instrument settings. The instrumental mass bias as well as potential isotopic fractionation due to Se loss during the chemistry was corrected using the double spike method. The Se isotope composition is reported using $\delta^{82/76}Se$ notation relative to the international reference material NIST SRM 3149 in ‰ units by multiplication with 1000:

$$\delta^{82/76}Se_{Sample} = \frac{\left(^{82}Se/^{76}Se\right)_{Sample}}{\left(^{82}Se/^{76}Se\right)_{NIST\ SRM\ 3149}} - 1$$

Selenium concentrations were obtained by double spike inversion. All $\delta^{82/76}Se_{NIST3149}$ are hereafter reported as $\delta^{82}Se$. Due to the lack of sulfide reference materials for Se isotope analysis, accuracy and precision of the measurement were evaluated by analyses of inter-laboratory standard MH 495 and repeated digestions of bulk pyrite powder (RP-1 to -11). The MH 495 yields a mean $\delta^{82}Se$ value of -3.23 ± 0.07 ‰ (2 s.d., n = 18), in agreement with literature values within uncertainty (Zhu et al., 2008; Carignan and Wen, 2007; Vollstaedt et al., 2016; Kurzawa et al., 2017; Labidi et al., 2018; Yierpan et al., 2018). The pyrite powder yields $\delta^{82}Se$ of -2.73 ± 0.09 ‰ (2 s.d., n = 11). In addition, the pyrite powder was measured together with a BHVO-2 (basaltic reference material, United States Geological Survey) that yields a $\delta^{82}Se$ value of 0.14 ± 0.04 ‰ (2 s.e., Table 1) and was published by Yierpan et al. (2018) as part of a study assessing the long-term BHVO-2 reproducibility in multiple analytical sessions over 6 months ($\delta^{82}Se$ = 0.18 ± 0.10 ‰, 2 s.d., n = 8).

Several authors reported that Se isotope measurements can suffer from severe memory effects, requiring very long washout times (Pogge von Strandmann et al., 2014) during the measurement or cleaning the HG chamber between measurement sessions (Vollstaedt et al., 2016). We did not observe such significant memory effects from the sample or double spike with a typical sample washout time of 6 min, as shown by subsequent resettled on-peak-zero signals and near constant $\delta^{82}Se$ values of bracketing standard solutions. This might be attributed to the relatively low Se amount required for our measurements.

### 3.5 Tellurium concentration measurements

High-precision Te concentrations were determined on an iCAP Qc quadrupole ICP-MS (ThermoFisher Scientific) linked with a hydride generator at the University of Tübingen, Germany, following the analytical protocol detailed by Yierpan et al. (2018). Briefly, aliquots of Te cuts were diluted to 0.15 - 0.5 ng $mL^{-1}$ Te (in 1 mL 2 M HCl) and introduced to the hydride generator together with continuous flows of 2 M HCl and reduction agent $NaBH_4$–NaOH to form hydride $H_2Te$. All sample unknowns (n = 8−10 in a session) were bracketed by 0.5 ng $mL^{-1}$ NIST SRM 3156 at the beginning (n = 4) and end (n = 2) of the analytical session. Every single analysis consisted of 820 measurements (420 after signal stabilization) of $^{125}Te$ and $^{126}Te$. Blank levels determined after a 2.5-min. washout typically generated < 3% of the $^{126}Te$ signal intensity obtained on a 0.5 ng $mL^{-1}$ solution. The obtained $^{125}Te/^{126}Te$ ratio was corrected for instrumental mass fractionation and used to calculate Te concentration using isotope dilution method. Note that all isobaric and polyatomic interferences generated from the analyte, carrier gas and cones (e.g., metal oxides, argides and hydrides) became insignificant after the on-peak-zero correction. The isotope dilution detection limit for Te is ~0.007 ng $mL^{-1}$. The long-term external reproducibility for Te concentration is ~2% (relative standard deviation; Yierpan et al., 2018).

### 3.6 Sulfur isotope analyses

Sulfur isotopes were measured on 0.1 mg aliquots from representative powder (RP-1 to 3) and from powdered pyrite microsamples (SPL-1 to 7) using a Finnigan Delta Plus XL mass spectrometer at the University of Tübingen, Germany. After removing these aliquots for S isotope analyses, all remaining RP and SPL sample materials were individually analyzed for Se isotope and Se and Te concentrations (see above). All $\delta^{34}S$ data are normalized to Vienna Canyon Diablo Troilite (V-CDT). For the analyses sulfur was converted to $SO_2$ in sealed tin capsules using an on-line NC 2500 elemental analyzer (CarloErba) with combustion temperatures of 1.050°C and a

separation column temperature of 100°C (Giesemann et al. 1994). Samples were calibrated to the $\delta^{34}S$ values of several in-house standards, such as the NBS 123 ($\delta^{34}S$ = 17.1 ‰), the NBS 127 ($\delta^{34}S$ = 20.3 ‰), the IAEA-S-1 ($\delta^{34}S$ = −0.3 ‰), and the IAEA-S-3 ($\delta^{34}S$ = 21.7 ‰), relative to the V-CDT. The long-term reproducibility is ±0.3 ‰ (2 s.d.) for $\delta^{34}S$.

3.7 In-situ trace element analyses

Three traverses through the pyrite from rim to core were investigated via LA-ICP-MS with a total of 34 analyzed points (Fig. 1c.). Furthermore, another 10 laser spots were placed in recrystallized pyrite surrounding inclusions. Analyses were performed on an Agilent 8800 QQQ ICP-MS coupled with an ESI 213 NWR laser ablation system in the Department of Earth Sciences at the University of Gothenburg. LA-QQQ analyses are guided using back-scattered electron (BSE) images, obtained with a SEM Hitachi at the Department of Earth Sciences, University of Gothenburg. This facility was also utilized for qualitative element abundances of inclusion phases. Laser spot size was set to 50 µm and ablation energy was ca. 4.9 J/cm$^2$. A measurement time of 60 seconds with 20 seconds of background and 40 seconds of laser ablation was applied. A washout time of 22 seconds in between measurements was allowed. Further details about the LA-QQQ setup can be found in Zack and Hogmalm (2016). The reaction gas $N_2O$ was used to avoid isobaric interferences. $N_2O$ is a highly potentate reaction gas, reacting efficiently with several key isotopes to form $MN^+$ or $MO^+$ ions. This allows elimination of argides ($MAr^+$, e.g., $Ar_2^+$) and doubly charged ions ($M^{2+}$,e.g., $^{160}Gd^{2+}$) interferences. Furthermore, it reduces isobaric interferences with a high ionization potential, like $^{126}Xe^+$. Consequently, accurate Se measurements in complex matrixes (e.g., sulfides, glasses) are possible by mass shifting Se isotopes 77, 78 and 80 to 93, 94, and 96, respectively. Tellurium can be measured on mass, using Te isotopes 125, 126 and 128. Additional isotopes measured were $^{24}Mg$ (on mass), $^{27}Al$ (on mass), $^{32}S$ (to mass 48), $^{39}K$ (on mass), $^{40, 44}Ca$ (to masses 56 and 60), $^{48,49}Ti$ (to masses 80 and 81) $^{56, 57}Fe$ (to masses 72, 73) $^{59}Co$ (on mass), $^{60}Ni$ (on mass),

312 $^{75}$As (to mass 91), $^{118}$Sn (on mass), $^{208}$Pb (on mass), and $^{209}$Bi (on mass). Average was calculated
313 when several isotopes were measured. The standard MASS-1 (Wilson et al., 2002) was used as a
314 primary standard, with concentrations determined by solution ICP-MS from Danyuchevsky et al.
315 (2011) (60.5 µg g$^{-1}$ for Se and 17.17.1 µg g$^{-1}$ for Te). The isotope $^{56}$Fe was used as an internal
316 standard (Gilbert et al., 2014) assuming ideal stoichiometry in pyrite. The data reduction software
317 Glitter (version 4.4.2) was used for quantification.

318 The sulfide standards AI-3 and Oreas 624-G (pressed nano-powder pellet from Oreas-624
319 powder) as well as the glass standards NIST SRM 610 (NBS 1979) and BAM-S005 were used as
320 secondary standards. Detection limits for pyrite using the above conditions are ca. 0.5 µg g$^{-1}$ for Se
321 and 0.07 µg g$^{-1}$ for Te. Sulfide standards AI-3 and Oreas 624-G are reproducible within 23% and
322 15% for Se, respectively, and the glasses are reproducible within -29% and -4% for Se,
323 respectively. Tellurium values reproduce within 2%, 16% and 29% for AI-3, Oreas 624-G and
324 NIST-SRM 610. It has to be stressed that literature values for Se and Te are hardly available, and
325 are partly based on LA-ICP-MS measurements, hardly suitable for thorough tests of accuracy.
326 Further ID-ICP-MS measurements are needed before matrix effects can be quantified for Se and Te
327 (for a strong indication of matrix effects between NIST glasses and MASS-1 see Wohlgemuth-
328 Ueberwasser et al. 2004). As a conservative value, we state an accuracy of 30% for Se and Te by
329 LA-QQQ for quantification of any matrix, and 23% for Se and Te when quantifying sulfides using
330 MASS-1 as a primary standard and $^{56}$Fe as an internal standard.

331

332 4. RESULTS

333

334 Back-scatter images reveal comparable textures as described by Alonso-Azcárate (1999), in
335 particular a high inclusion density in most parts of the pyrite, with phyllosilicates, quartz, dolomite
336 and chloritoid occurring in order of abundance. Despite careful investigations, anhydrite inclusions
337 have not been observed in the studied pyrite. Furthermore, we observed inclusions sizes down to

~0.1 µm (limit of spatial resolution of SEM). All LA-ICP-MS data are summarized in the Eletronic Appendix. A significant proportion of those nano-inclusions are rich in Ti, a feature observable in the high apparent high Ti content of most of the pyrite analyses (1000-5000 µg $g^{-1}$; see below). However, also observed a second generation, ranging between 100-500 µm. Several types of inclusions have been described, including phyllosilicates (illite and chlorite), quartz, chloritoid chalcopyrite, sphalerite, iron oxides and occasionally calcite, dolomite and anhydrite. Recrystallized pyrite are revealed in BSE images, featured by a lack of those nano-inclusions and euhedral crystal boundaries towards inclusion phases. LA-QQQ spot analysis of these pyrites result in very low Ti contents (< 20 µg $g^{-1}$).

Traverses across the investigated pyrite by LA-QQQ show a complex, though systematic zoning profile (Table in Electronic Appendix). The most striking feature is the decoupling of most analyzed elements, with distinct maxima for Mg, Pb and Bi (zone 1), Co (zone 2), K and Al (zone 3), Te (zone 4) and Se (zone 5) more or less clearly distinguishable in all three profiles. We suspect that most of those patterns can be explained by changes in occurrence and/or abundance of nano-inclusions, as inclusion-free, second generation pyrites are often virtually free of most analyzed elements, except Ni and Se. We suspect that zone 1 and zone 3 are particularly rich in chlorite and illite nano-inclusions, respectively. We cannot rule out that, elements like Co, Te, Pb and Bi are in the crystal structure of pyrite and only leached out during formation of the secondary generation pyrite. In any case, there is strong indication that, unlike Te, Se (and hence information on Se isotopes) are bound in the pyrite crystal structure.

A comparison of Se and Te data obtained via LA-QQQ and isotope dilution (MC-) ICP-MS is shown in Fig. 2. The representative powder (RP-1 to 11) yields an average S content of 50.6 ± 0.8 wt.% S, Se content of 5.08 ± 0.08 µg $g^{-1}$ Se, and Te content of 0.21 ± 0.005 µg $g^{-1}$ Te (all 1 s.d.). Average $\delta^{34}S$ value is -5.4 ± 0.3 ‰, which is in good agreement with previously published $\delta^{34}S$ data (Alonso-Azcárate et al., 1999b). Average $\delta^{82}Se$ value is -2.73 ‰ ± 0.09 ‰ (2 s.d.) (Fig. 3a). This

363 includes analyses of powder from 50 to 5 mg digested material, corresponding to a total Se mass of
364 as low as 25 ng and further dilution of samples for analyses down to 15 ng $g^{-1}$.

365 Two 50 mg sample digests of unrepresentative powder UP-1a, b prepared from less than 1 g
366 starting material off one corner of the pyrite cube yield Se contents of 4.40 and 4.46 µg $g^{-1}$ Se and
367 $\delta^{82}$Se values of -2.13 ‰ and -2.15 ‰, respectively. Although [Se] and Se isotopic values of both
368 analysis (UP-1a and b) are in good agreement, they differ from the bulk pyrite average RP value.
369 Another 2 x 50 mg sample digests, also prepared from less than 1 g starting material but from
370 another side of the same pyrite cube (UP-2a, b), yield 4.97 and 4.94 µg $g^{-1}$ Se and a markedly
371 lighter Se isotope composition with $\delta^{82}$Se values of -1.31 ‰ and -1.30 ‰, respectively (Fig. 3a).
372 These values are again in good agreement but differ from UP-1a, b and the bulk pyrite average
373 obtained from RP-1 to 11.

374 Individually digested pyrite microsamples (SPL-1 to 10) cut from different areas of the cube
375 crystal show highly variable Se contents between 3.58 to 6.54 µg $g^{-1}$ and 0.182 to 0.378 µg $g^{-1}$ Te.
376 Of these microsamples samples SPL-1 to 7 show a range in $\delta^{34}$S between -7.1 to -4.4 ‰ and
377 between -4.48 to -0.39 ‰ in $\delta^{82}$Se (Fig. 3a). No systematic trend between isotopic compositions
378 and concentrations or elemental ratios is observed, but all data of individually digested and
379 analyzed pyrite microsamples scatter around the representative bulk pyrite value, respectively (Fig.
380 3c, d). Concentrations of Se and Te are highly reproducible (~2% 1 s.d.) for representative powder
381 (RP) material and agree well with average values obtained from in-situ LA-ICP-MS analyses. In
382 any case, for solution ICP-MS analyses, both Se and Te concentrations of analyzed solutes were
383 well above the isotope dilution detection limits of ~0.05 and ~0.007 ng $g^{-1}$, respectively. This is
384 because of the generally higher sample amount required for Se isotope measurements (~15 ng Se)
385 compared to concentration analyses (~0.5 to 1 ng Se and Te, Navajún pyrite Se/Te = 10) in 1 ml
386 sample solution. In addition to reference materials analyzed, the good agreement between average
387 laser and isotope dilution Se and Te data further indicates that both analytical methods are accurate.
388 Nevertheless, laser analyses reveal strong Se and Te distribution heterogeneities within the Navajún

389 pyrite. While [Se] variability of the homogenized RP sample was ~ 2% (1 s.d.), variability of
390 individual LA-ICP-MS spots and individual pyrite microsamples (SPL) are 31% and 41%
391 respectively. A much higher variability of [Te] within LA-ICP-MS and SPL samples compared to
392 RP samples support observations made for [Se]. This shows a strong Se and Te heterogeneity and
393 rather low overall concentrations compared to other hydrothermal pyrites. However, with a
394 calculated metamorphic temperature of 370°C (Alonso-Azcárate et al., 1999a) low Se
395 concentration are expected since Se incorporation into pyrite is temperature depended and
396 will decrease with increasing temperatures (Keith et al 2018).
397 Interestingly, a clear decoupling between S and Se isotopic signatures can be resolved (Fig.
398 4a). This shows variations in Se isotopes at confined S isotopic values and vice versa: For given
399 highest and confined $\delta^{34}S$, $\delta^{82}Se$ range over ca. 4 ‰. In contrast, $\delta^{34}S$ extend to lower values by 2
400 ‰ only for the highest $\delta^{82}Se$.
401
402
403 5. DISCUSSION
404
405 5.1 Microscale elemental and isotopic heterogeneity
406
407 Our average S isotope value for RP-1 to 3 ($\delta^{34}S$ = -5.4 ± 0.3 ‰) is lower than the reported
408 average reported for Navajún pyrite subgroup A, albeit within it's range ($\delta^{34}S$ = -2.4 ± 3 ‰),
409 compared to values for pyrites from the entire Cameros Basin ($\delta^{34}S \approx$ -10 to 14 ‰) (Alonso-
410 Azcárate et al., 1999a). Likewise, S isotope data for our individually analyzed microsamples (SPL-1
411 to -7; $\delta^{34}S$ = -7.1 to -4.4 ‰) are comparable to the microscale variation previously reported for
412 another Navajún pyrite ($\delta^{34}S$ = -6.2 to -4.7 ‰, Alonso-Azcárate et al., 1999a). In addition to the
413 above noted accuracy and reproducibility for reference materials we thus infer that a microscale S
414 isotope heterogeneity is indeed resolved within our pyrite specimen. This $\delta^{34}S$ heterogeneity is also

similar to those previously reported for each of the other individual deposits within the Cameros Basin. As for these other deposits (Alonso-Azcárate et al., 1999a), we can also infer variable proportions of isotopically light SD-derived vs. isotopically heavy TSR-derived S that contributed to our pyrite. Hence, while the investigation of different pyrite samples may have extended the overall S isotope range, our individual pyrite crystal shows already sufficient microscale variations in order to evaluate the role and variable proportions of SD-TSR contributions. This lends a representative character to our specimen regarding the nature of these different involved processes and provides the possibility to assess the role of these processes on combined S-Se isotope systematics.

Se isotope measurements of 11 individual sub-samples, which can be considered representative (RP) of the bulk pyrite, yielded a reproducibility of 0.09 ‰ (2 s.d.) on $\delta^{82}$Se. These measurements include digested starting materials with total Se contents between ~25 to ~250 ng and analyses on diluted solutions as low as 15 ng $g^{-1}$. Measurement conditions were optimized for signal intensities that correspond to 15 to 30 ng total Se (see above). In other words, most samples required strong dilution and even samples with as low as 15 ng total Se, derived from ~3 mg of Navajún pyrite material with a concentration of ~5 µg $g^{-1}$ Se, can be measured accurately.

The good reproducibility of RP samples is in strong contrast to the large variability of UP and SPL samples. $\delta^{82}$Se values for individual microsamples show a large scatter of over 4.4 ‰, irrespective of each amount used (17 to 67 ng total Se). In fact the highest and lowest $\delta^{82}$Se was obtained for digested SPL amounts of 65 ng and 28 ng, respectively, well above that of the lowest RP of 27 ng (Fig. 2b) Moreover, given that the internal error on individual SPL measurements with individual signal intensities is similar to those used for RP analyses, it is likely that the $\delta^{82}$Se variations of SPL analyses are unrelated to analytical bias rather than a natural effect. In other words, as for S isotopes, our analytical method resolves actual Se isotope differences between different areas of the pyrite crystal. It is further noteworthy that this Se isotope heterogeneity is well outside our analytical reproducibility of 0.09 (2 s.d.) and significant in terms of its range of over 4.4

441 ‰ in $\delta^{82}$Se, the latter exceeding even range of $\delta^{34}$S of 2.7 ‰. In summary, our analytical technique
442 is demonstrated to be sufficiently accurate for homogeneous sulfide materials and, where such
443 material is heterogeneous, the method is capable to resolve Se isotopic variations well beyond an
444 uncertainty of 0.09 ‰ (2 s.d.). Therefore we conclude that, as for Se and Te contents and S isotope
445 signatures, the herein analyzed Navajún pyrite specimen shows a strong natural Se isotope
446 heterogeneity at the microscale.
447
448 5.2 Absence of S-Se isotope decoupling generated during Navajún pyrite growth
449
450 In addition to a significant Se heterogeneity, our dataset also reveals S and Se isotopic
451 decoupling within the analyzed pyrite (Fig. 3a). Se isotope variations over 4.4 ‰ in $\delta^{82}$Se are
452 observed between pyrite microsamples where $\delta^{34}$S values remain rather confined to the highest $\delta^{34}$S
453 values of the dataset. In contrast, $\delta^{34}$S variations of more than 2.7 ‰ are observed between these
454 microsamples where $\delta^{82}$Se remain relatively constant at their highest values. In other words, the
455 observed S and Se isotope decoupling has a complementary nature. This is the first time such a
456 systematic is observed in natural pyrite. Both S and Se are chalcophile and both incorporate into the
457 pyrite structure (e.g., Diener et al., 2012) where Se pyrite content can be controlled by changing
458 Se/S ratio of the fluid, Se/S fractionation by different temperature or changing redox conditions
459 during pyrite formation (Layton-Matthews et al 2008, Huston et al., 1995). Both isotope systems
460 are redox sensitive with light isotopes being preferentially reduced and reduction of Se and S
461 species producing strong isotopic fractionations (see Johnson 2004 and references therein). A
462 significant difference is that, reduction-related Se isotopic fractionations occur at higher Eh
463 potentials and over a larger Eh interval compared to S. For instance, at a pH of 7 the reduction from
464 $Se^{6+}$ to $Se^{4+}$ and finally to $Se^{0}$ occur between 0.8 V and 0.4 V, where $S^{6+}$ remains stable (Fig. 4b).
465 Reduction of $S^{6+}$to $S^{2-}$ occurs only below Eh of -0.2 V, slightly below the upper boundary of $Se^{2-}$
466 stability. Hence, starting with oxidized species, reduction-related Se isotope fractionation occurs

before reduction-related S isotope fractionation even begins. This provides a potential for more pronounced Se than S isotope fractionation over a larger redox interval at elevated Eh, while more pronounced S than Se isotope fractionations may occur over a smaller redox interval and lower Eh. The observed S-Se isotope decoupling in our Navajún pyrite could therefore be related to the higher redox potential of Se than S species if both elements were derived from the same sources.

Possible origins of redox-related Se isotope fractionation and hence decoupling of sulfur and selenium isotopes include reduction-driven fractionation during sorption and incorporation during crystal growth (see below). Alternatively, as invoked for S in this case (Alonso-Azcárate et al., 1999a), previously produced differences in sulfur and selenium isotope signatures between two fluids are subsequently mixed in variable proportions during pyrite growth (see 5.3).

Significant isotope fractionation of up to ~9 ‰ in $\delta^{82}Se$ has been reported due to Se reduction in sorption experiments of $Se^{4+}$ and $Se^{6+}$ to ferrous sulfides at 25 °C (Mitchell et al., 2013). In theory, the reduction of Se during sorption to pyrite could explain the more pronounced incipient Se isotopic fractionation compared to S. However, in the Cameros Basin the principal S source of the S-bearing fluids is $H_2S$ (Alonso-Azcárarate et al., 1999a) and hence Se would be present as $H_2Se$ and already reduced prior to sorption to pyrite. Moreover, a temperature of ca. 370°C during Navajún pyrite formation (Alonso-Azcárarate et al., 1999b), is considerably higher compared to those in the experiments of Mitchell et al. (2013). Hence, the relatively high temperature during Navajún pyrite growth is believed to inhibit S isotope fractionation (Machel et al., 1995) and likely prevents Se isotope fractionation as well. In agreement with this, the absence of zoning-dependent S isotope variation in the Navajún pyrite has previously been attributed to a lack of systematic isotopic fractionation related to crystal growth, rather than mirroring the fluid signature that delivered S (Alonso-Azcárarate et al., 1999a). Moreover, as for S, the lack of concentration-dependent Se isotope variation (Fig. 2c) does not suggest any systematic isotope decoupling related to variable Se incorporation into the pyrite caused by changing temperature of redox conditions during pyrite formation. A hypothetical [Se] vs. $\delta^{82}Se$ correlation could of course

493 be obscured by variably dilution effects of minor S and Se-bearing inclusions in some analyzed
494 microsamples. However, the pyrite microsamples analyzed were cut from the inclusion-poorer outer
495 area of the pyrite cube. Also, in contrast to Te, which shows significant concentrations in the
496 heterogeneously distributed inclusions within the pyrite, (Table S1), Se is not concentrated in such
497 inclusions and therefore rather homogeneously incorporated in the pyrite matrix itself. Moreover,
498 compared to the pyrite matrix, dilution effects by minor S and Se bearing inclusions have negligible
499 effect on the S and Se isotope composition of a given microsample and cannot lead to the observed
500 S and Se isotope decoupling.
501 In summary, as previously deduced for S, Se isotope heterogeneity together with a S and Se
502 isotope decoupling in our Navajún pyrite sample seems not to have been generated during crystal
503 growth. Instead, it is likely that the systematics are in fact a record of previously established
504 isotopic signatures. Further assessment of Se isotope systematics and S and Se isotope decoupling
505 benefits from previous constraints on Navajún pyrite formation and S isotope evolution models.
506
507 5.3 Sources of S - Se and existing model for S isotope signatures of Navajún pyrites
508
509 A survey of all pyrites occurring in the Cameros Basin reveals a range of $\delta^{34}S$ from -10 to +14 ‰
510 with one Navajún pyrite sub-population (n = ??) showing a more restricted $\delta^{34}S$ range between -5
511 and 0 ‰ (Alonso-Azcárarate et al., 1999a). $\delta^{34}S$ variations between -7.1 and -4.4 ‰, recorded in
512 individually analyzed microsamples (Fig. 3a) relative to the average bulk pyrite $\delta^{34}S$ value (RP
513 average = -5.4 ± 0.3 ‰) would thus reflect ca. 60% of the variation in one Navajún pyrite sub-
514 population and still ca. 10% of the overall S isotopic variation across all pyrite populations in the
515 Cameros Basin. These variations are not created by ambient temperature, pH and Eh conditions
516 during crystal growth but as a result of changing mixing proportions of two fluids with different S
517 isotopic signatures during pyrite formation. The previously proposed model to explain S isotope
518 variations of the Navajún pyrites (Alonso-Azcárarate et al., 1999a) is schematically shown in Fig.

519 3c and involves two mineral sources (source A and source B) with distinct S (and likely Se) isotopic
520 signatures, Se and S redox states and Se/S ratios. Decomposition of these sources will lead to fluids
521 with characteristic S and Se signatures, contributing the dissolved S and Se to variable proportions
522 during pyrite growth. These initial isotopic signatures change in the respective fluid due to
523 fractionation processes after scavenging and during mobilization of S (and Se) from either source.
524 Finally, both fluid types contribute their modified isotopic signatures to variable proportions to the
525 pyrite during its growth. The two fractionation processes were previously described as follows:
526 Sulfide dissolution (SD) of sedimentary pyrites with $\delta^{34}S < 0$ ‰ (source A) by a slightly oxidized
527 fluid led to subtle oxidation and later reduction to produce an $H_2S$ fluid. The rather modest redox
528 variation (i.e. reduction from moderate Eh) nevertheless led to kinetic S isotope fractionation
529 (Alonso-Azcárarate et al., 1999a) to produce a light S isotopic composition and explains the low
530 $\delta^{34}S$ pyrite endmember (ca. -10 ‰). On the other hand, thermochemical sulfate reduction (TSR) of
531 a gypsum deposit with a very high $\delta^{34}S$ value of ca. +12 ‰ (source B) is believed to be the
532 isotopically heavy end-member. Depending on temperature it has been shown that during TSR
533 substantial kinetic S isotopic fractionation of $\delta^{34}S > 10$ ‰ between $SO_4^{2-}$ and $H_2S$ can be archived
534 (Meshoulam et al., 2016), which readily explains the TSR-derived isotopic Navajún pyrite
535 endmember with $\delta^{34}S = -4.7$‰. Mixing of these endmember fluid signatures in variable proportions
536 has therefore been invoked to explain the range of $\delta^{34}S$ in the respective Navajún pyrite population
537 (Alonso-Azcárarate et al., 1999a) and may also explain the range seen in microsamples of our
538 specimen.

539 Our new Se isotope data and the observed S and Se isotope decoupling could be readily
540 interpreted within the same model as for S if we assume that Se is derived from the same two
541 sources as S. This assumption is straightforward, as most sulfide deposits are of course enriched in
542 Se to different degrees, due to its chalcophile character, leading to variable S-Se ratios. Gypsum, for
543 instance has lower Se concentrations and therefore an overall higher S-Se ratio (factor 20 up to 200)
544 compared to sulfide (USEPA, 1996; Kabata-Pendias, 1998). Indeed, our inferred TSR fluid source

must have S-Se ratios that are 20-200 times higher than that of our SD fluid source. (see model in section 5.4). Thus, the different S-Se ratios are in agreement with the gypsum deposits and sulfides that are invoked as respective sources here (Alonso-Azcárarate et al., 1999a) and may be an additional argument for the same sources of both S and Se. On the other hand, it is unlikely that Se is derived from a third source without any additional S. Such a third S endmember would then likely obscure the previously inferred mixing models (Alonso-Azcárarate et al., 1999a) and the dichotomy of S and Se isotope signatures observed in our pyrite. Also, no correlation is observed between Se contents and isotope variation towards the TSR endmember, where it would be most expected if this Se isotope variation would be derived from a third source and be dependent on the amount of additional Se introduced. In summary, it is very plausible to assume that, although to different extents, S and Se are derived from the same gypsum and sulfide sources and even more likely that both S and Se were subject to the same reduction processes in fluids that transported these elements to the site of pyrite formation.

### 5.4 Constraints on reduction processes in fluids that transport S-Se from source to pyrite

The proposed mixing of relatively high $\delta^{34}S$ TSR- with low $\delta^{34}S$ SD-bearing fluids coincides with a reverse trend of low $\delta^{82}Se$ TSR- and high $\delta^{82}Se$ SD- signatures (Fig. 3a). Starting from an isotopically heavy $\delta^{34}S$ sulfate reservoir Se yielding a $\delta^{82}Se$ value close to seawater the reduction of Se species during TSR can occur well before reduction of S species. This is due to the higher redox potential of Se species compared to those of S (Fig. 3b) and provides a scenario for the large Se isotope variations at relatively constant S isotope signatures. In this case, the high $\delta^{34}S$ - low $\delta^{82}Se$ TSR endmember signature captures the accumulated fractionations associated with reduction from $Se^{6+}$ to $Se^{4+}$ and $Se^{2-}$ as well as from $SO_4^{2-}$ to $H_2S$ (TSR arrow in Fig.3b).

On the other hand, the low $\delta^{34}S$ - high $\delta^{82}Se$ SD endmember produced from source A can be reconciled with the invoked kinetic S isotope fractionation (Kajiwara et al., 1981; Yamamoto,

571 1984), if the proposed sulfur dissolution (SD) by $H_2O$ and kinetic S isotope effect occurred under
572 low and confined Eh conditions, thus not requiring large redox variations that could trigger
573 significant redox-related Se isotope fractionations (SD arrow in Fig. 3b). In other words, Se is
574 already reduced in the sedimentary pyrite in source A and remains reduced during SD so that this
575 isotopically light Se reflects that of the source, whereas S requires only a subtle oxidation and
576 subsequent reduction to explain the invoked kinetic S isotopic effect. Indeed the rather constant
577 $\delta^{82}$Se values close to zero in the highest SD-bearing pyrite microsamples ($\delta^{82}$Se = -0.4 ‰) suggest
578 very little, if any, reduction–related Se isotope fractionation compared to TSR. In order to fully
579 resolve this scenario, the primary sedimentary sulfide source A (Alonso-Azcárarate et al., 1999a)
580 and their reaction products need to be analyzed for Se isotopes, which is beyond the scope of this
581 study. At this point we focus on the complementary relative isotope variations and argue that the
582 high and rather constant $\delta^{82}$Se values with decreasing $\delta^{34}$S values are well reconciled by variable
583 contribution of different $H_2S$ rich fluid sources during pyrite growth and reduction following subtle
584 oxidative fluid scavenging from the SD source A, in contrast to the TSR source B where large
585 reduction from fully oxidized gypsum sources are likely (Fig. 3b).

586 To test if variable proportions of SD-TSR can indeed explain not only the S but also the Se
587 isotopic composition and complementary S and Se isotope signatures of the Navajún pyrite, we
588 calculate variable mixing of SD-TSR fluid signatures (Fig. 4). The model calculation itself together
589 with all values used can be found in the Electronic Appendix to this study. For S we use the most
590 positive and negative $\delta^{34}$S values of our pyrite microsamples as captured TSR and SD endmembers,
591 repectively ($\delta^{34}$S = -4.7 and -10 ‰). This agrees well with the range of Navajún pyrite
592 subpopulation A ($\delta^{34}$S = -5 and -10 ‰; Alonso-Azcárarate et al., 1999a) to which our specimen
593 belongs. We further use the most negative and positive $\delta^{82}$Se values of our analyzed microsamples
594 as TSR and SD endmembers, respectively ($\delta^{82}$Se = -4.4 and -0.4 ‰). It is noteworthy that the TSR
595 $\delta^{82}$Se endmember of $\delta^{82}$Se = -4.4 ‰ used in our model is not just an outlier, as another
596 microsample not analyzed for S confirms the occurrence of such low Se isotope signatures at the

597 microscale (Fig. 1b). The S/Se ratios of either source is unknown, but was set to 1 for the SD-
598 derived fluid and modified for the TSR–derived fluid to obtain a best fit model of the
599 complementary S-Se isotopic evolution trend with progressive admixture of the TSR to the SD
600 component. To cover the hyperbolic trend in our dataset the S/Se ratio in the TSR fluid is at least
601 20 – but may be as much as 200 – times higher than that of the SD endmember. As discussed in the
602 previous section this may also be an additional argument for gypsum as one source for S and Se as
603 gypsum has the required high S-Se ratios (USEPA, 1996; Kabata-Pendias, 1998). More systematic
604 S and Se isotope studies of deposits and fluid veins across the Cameros Basin would clearly provide
605 further constraints on the exact endmember signatures.
606 In summary, mixing of fluids with variable S/Se that contribute two complementary S and
607 Se isotope signatures can be reconciled with higher redox potential of Se relative to S and markedly
608 different sensitivities of either isotope system to subtle or pronounced reduction, respectively.
609 Hence, for given pH that is most likely constant under open system conditions (see section 2), both
610 maximum and minimum Eh are more firmly estimated by S and Se isotope systematics. This makes
611 a combination of S-Se isotope investigation very useful for redox studies in modern environments
612 and the geological rock record.
613
614 5.5 Potential of coupled S and Se isotope systematics for palaeo-redox studies
615
616 This study demonstrates the potential for combined S and Se isotope analyses to provide new
617 information about the history of redox conditions in fluids that supplied S and Se to a single pyrite.
618 In this case, the large Se isotope variations at constant $\delta^{34}S$ values indicate larger redox variations
619 as can be inferred from S isotopes alone. A straightforward application of this method is, however,
620 to analyze individual diagenetic pyrites from bulk sediments, which could not previously be
621 analyzed for Se with this high precision. In addition to bulk sediments, our new approach allows
622 investigating the S and Se isotopic composition of different sulfide minerals directly via micro-

623 sampling/micro-drilling. The possibility to detect potential sulfide-scale Se isotope variations and to
624 resolve even subtle $\delta^{82}$Se differences between sulfide populations opens up new possibilities. It is
625 possible to scrutinize if a given bulk rock bulk sulfide $\delta^{82}$Se signature is in fact a mixture of various
626 fluids. A systematic S and Se isotope decoupling could then indicate if these fluids are derived from
627 different precursor S reservoirs under different redox conditions. In combination with an in situ
628 trace element investigation for sedimentary pyrite (Large et al., 2014), S-Se isotope studies might
629 gain important additional information about the diagenetic evolution of ancient sedimentary sulfide
630 and the prevailing environmental redox conditions at their time of crystallization. For instance, the
631 Great Oxidation Event between 2.45 to 2.32 Ga ago (GOE; Holland, 2002; see Lyons et al., 2014
632 for a recent review) is linked to the disappearance of mass-independent fractionation of sulfur
633 isotopes (MIF-S), indicating that atmospheric oxygen levels in the post-GOE atmosphere were high
634 enough to prevent the photochemical dissociation of volcanic sulfur species (Farquhar et al., 2000).
635 However, the preservation of MIF-S signals in sulfide inclusions of modern ocean island basalts
636 (OIBs; Cabral et al., 2013) as well as independent quantitative modeling constraints (Reinhard et
637 al., 2013) provide strong evidence that MIF-S signals can be subject to sedimentary recycling at the
638 crustal and mantle scale and are only erased after multiple cycles of weathering and dilution under
639 fully oxic conditions. As for these OIBs, it is possible that recycled MIF-S signatures are hosted by
640 different minerals (e.g. diagenetic vs. detrital sulfides) and mixed to produce a bulk rock signature
641 in sediments. Analyses of both S and Se isotopes of individual sulfides in these rocks would thus
642 help to assess whether systematic S and Se isotope decoupling attest to different populations or
643 generations of sulfides. Obviously, $^{33}$S needs to be measured in addition to $^{32}$S and $^{34}$S, but was not
644 tested here, as MIF-S signatures would indeed be very surprising in the Cretaceous Navajún pyrite.
645 Similar to trace element studies in sedimentary pyrite (Large et al., 2014), further applications
646 encompass critical time periods in Earth's geological history such as potential pre-GOE whiffs of
647 oxygen (Anbar et al., 2007), the muted MIF-S signature in the Mesoarchean or the second
648 significant atmospheric $O_2$ increase to the near-modern $O_2$ levels in the Neoproterozoic (see also

649 Fig. 5a). Sulfur isotope excursions may be followed by excursions in $\delta^{82}Se$, indicating a minimum
650 $O_2$ increase (Fig. 5b, c). On the other hand, constant $\delta^{82}Se$ over periods of S isotope excursions may
651 place an upper limit on possible $O_2$ levels at the time (Fig. 5d, e). If, however, $\delta^{82}Se$ signatures
652 show significant variations where $\delta^{34}S$ are rather constant, a lower limit on $O_2$ drop could be
653 constrained (Fig. 5f, g). It is evident that changes of porewater pH could play an additional effect.
654 However, the higher redox potential of Se over S persists over the entire range of pH, therefore not
655 principally limiting a coupled S and Se isotope investigation of (palaeo-) redox variations.
656 Moreover, the magnitude of Se isotope fractionation seems independent from its concentration
657 (Ellis et al., 2003), which is different for S (Habicht et al., 2002). Due to a relatively short seawater
658 residence of Se, it is likely that a S and Se isotope decoupling relates to local conditions and
659 therefore requires small-scale investigation of individual minerals to disentangle a likely mixture of
660 different signatures generated in different areas at a given time. Although distinctions between
661 abiotic and biological causes cannot be made solely on the basis of Se isotope variations (see also
662 Johnson and Bullen, 2003), the decoupling of S and Se isotopes captured in a single sulfide mineral
663 allow, for a given pH, more detailed understanding of redox fluctuations in the geological rock
664 record. Moreover, as both S and Se both are enriched in igneous and hydrothermal sulfides, the
665 combined S and Se isotope approach can be expanded to Earth's igneous reservoirs.
666
667 6. CONCLUSIONS
668
669 This study presents the first combined microscale S and Se isotope investigation of pyrite. Precise
670 selenium isotope analyses of individual pyrite microsamples with Se concentrations down to 5 ng
671 are possible. In combination with conventional S isotope analyses these measurements allow novel
672 high-resolution, high precision S and Se isotope data acquisition on pyrite. Our case study of
673 Najavún pyrite from the Cameros Basin, Spain, shows a $\delta^{82}Se$ range of 4.4 ‰ and a $\delta^{34}S$ range of
674 2.7 ‰. Together with LA-ICPMS elemental data we demonstrated that these signatures are

675 unrelated to incorporation into the pyrite structure during crystal growth. Rather, these signatures
676 were mixed prior to pyrite formation and therefore mirror different magnitudes of reduction in the
677 $H_2S$ and $H_2Se$ fluid sources that supplied both S and Se. Ultimately, the Se and S isotope
678 decoupling is related to the higher redox potential of Se compared to S and allows more robust
679 constraints on minimum oxidative and reductive conditions in the fluids that supplied these
680 elements.

681 This case study shows that combined S and Se isotope studies may provide more refined
682 constraints on source redox histories captured in sulfides. Besides the possibility to resolve
683 variations within such sulfides, comparisons between individual sulfides are possible and extend the
684 possibility to study redox variations beyond the whole rock scale. We suggest combined S and Se
685 isotope analyses in pyrite as a new powerful paleo-redox proxy for studying Earth's redox evolution
686 on the mineral and micro-scale.

687

688 ## 7. ACKNOWLEDGEMENTS

689

690 This work was funded by an ERC Starting Grant ($O_2$RIGIN, 636808) to S. König. Bernd
691 Steinhilber is thanked for assistance during the S analyses. Mike Babechuk shared constructive
692 ideas. We thank two anonymous reviewers for very thoughtful comments and Edward Ripley for
693 editorial handling of the manuscript.

694

695 ## 8. REFERENCES

696

697 Alonso-Azcárate, J., Rodas, M., Bottrell, S.H., Raiswell, R., Velasco, F. and Mas, J.R. (1999a).
698 Pathways and distances of fluid flow during low-grade metamorphism: evidence from pyrite
699 deposits of the Cameros Basin, Spain. Journal of Metamorphic Geology, 17(4), pp. 339-348.
700 doi:10.1046/j.1525-1314.1999.00202.x

Alonso-Azcárate, J., Boyce, A.J., Bottrell, S.H., Macaulay, C.I., Rodas, M., Fallick, A.E. and Mas, J.R. (1999b). Development and use of in situ laser sulfur isotope analyses for pyrite-anhydrite geothermometry: An example from the pyrite deposits of the Cameros Basin, NE Spain. Geochimica et Cosmochimica Acta, 63(3-4), pp. 509-513. doi.org/10.1016/S0016-7037(99)00022-8

Alonso-Azcárate, J., Bottrell, S.H. and Tritlla, J. (2001). Sulfur redox reactions and formation of native sulfur veins during low grade metamorphism of gypsum evaporites, Cameros Basin (NE Spain). Chemical Geology, 174(4), pp. 389-402. doi.org/10.1016/S0009-2541(00)00286-2

Anbar, A.D., Duan, Y., Lyons, T.W., Arnold, G.L., Kendal. B., Creaser, R.A., Kaufman, A.J., Gordon, G.W., Scott, C., Garvin, J., Buick, R. (2007). A whiff of oxygen before the Great Oxidation Event? Science, 317, pp. 1903-1906

Cabral, R.A., Jackson, M.G., Rose-Koga, E.F., Koga, K.T., Whitehouse, M.J., Antonelli, M.A., Farquhar, J., Day, J.M.D. and Hauri, E.H. (2013). Anomalous sulphur isotopes in plume lavas reveal deep mantle storage of Archaean crust. Nature, 496, pp. 490–493, doi:10.1038/nature12020

Carignan, J. and Wen, H.J. (2007). Scaling NIST SRM 3149 for Se isotope analysis and isotopic variations of natural samples. Chemical Geology, 242(3-4), pp. 347-350. doi.org/10.1016/j.chemgeo.2007.03.020

Casquet, C., Galindo Francisco, M.d.C., González Casado, J.M. and Alonso Millán, Á. (1992). El metamorfismo en la Cuenca de los Cameros. Geocronología e implicaciones tectónicas. Geogaceta, 11, pp. 22-25

Clark, S.K. and Johnson, T.M. (2010). Selenium Stable Isotope Investigation into Selenium Biogeochemical Cycling in a Lacustrine Environment: Sweitzer Lake, Colorado. Journal of Environmental Quality, 39(6), pp. 2200-2210. doi.org/10.2134/jeq2009.0380

Danyushevsky, L., Robinson, P., Gilbert, S., Norman, M., Large, R., McGoldrick, P. and

727 Shelley, M. (2011). Routine quantitative multi-element analysis of sulfide minerals by laser
728 ablation ICP-MS: Standard development and consideration of matrix effects. Geochemistry:
729 Exploration, Environment, Analysis, 11(1), pp. 51-60. doi.org/10.1144/1467-7873/09-244
730 Diener, A., Neumann, T., Kramar, U. and Schild, D. (2012). Structure of selenium incorporated
731 in pyrite and mackinawite as determined by XAFS analyses. J Contam Hydrol, 133, pp. 30-
732 9. doi.org/10.1016/j.jconhyd.2012.03.003
733 Ellis, A.S., Johnson, T.M., Herbel, M.J. and Bullen, T.D. (2003). Stable isotope fractionation of
734 selenium by natural microbial consortia. Chemical Geology, 195(1-4), pp. 119-129.
735 doi.org/10.1016/S0009-2541(02)00391-1
736 Farquhar, J., Bao, H.M. and Thiemens, M. (2000). Atmospheric influence of Earth's earliest
737 sulfur cycle. Science, 289(5480), pp. 756-758. doi.org/10.1126/science.289.5480.756
738 Giesemann, A., Jaeger, H.J., Norman, A.L., Krouse, H.R. and Brand, W.A. (2002). Online
739 Sulfur-Isotope Determination Using an Elemental Analyzer Coupled to a Mass
740 Spectrometer. Analytical Chemistry, 66(18), pp. 2816-2819. doi.org/10.1021/ac00090a005
741 Gilbert, S.E., Danyushevsky, L.V., Goemann, K. and Death, D. (2014). Fractionation of
742 sulphur relative to iron during laser ablation-ICP-MS analyses of sulfide minerals:
743 implications for quantification. Journal of Analytical Atomic Spectrometry, 29(6), pp. 1024-
744 1033. doi.org/10.1039/c4ja00012a
745 Habicht K. S., Gade M., Thamdrup B., Berg, P., Canfield, D.E. (2002). Calibration of Sulfate
746 Levels in the Archean Ocean. Science 298, 2372–237. doi:10.1126/science.1078265
747 Hein, J.R., Koschinsky, A. and Halliday, A.N. (2003). Global occurrence of tellurium-rich
748 ferromanganese crusts and a model for the enrichment of tellurium. Geochimica et
749 Cosmochimica Acta, 67(6), pp. 1117-1127. doi.org/10.1016/S0016-7037(00)01279-6
750 Herbel, M.J., Johnson, T.M., Oremland, R.S. and Bullen, T.D. (2000). Fractionation of
751 selenium isotopes during bacterial respiratory reduction of selenium oxyanions. Geochimica
752 et Cosmochimica Acta, 64(21), pp. 3701-3709. doi.org/10.1016/S0016-7037(00)00456-7

753 Holland, H.D. (2002). Volcanic gases, black smokers, and the Great Oxidation Event.
754 Geochimica et Cosmochimica Acta, 66(21), pp. 3811-3826. doi.org/10.1016/S0016-
755 7037(02)00950-X
756 Ferry, J.M. (1981). Petrology of graphitic sulfide-rich schists from South-central Maine; an
757 example of desulfidation during prograde regional metamorphism. American Mineralogist,
758 66(9-10), pp. 908-930.
759 Johnson, T.M. (2004). A review of mass-dependent fractionation of selenium isotopes and
760 implications for other heavy stable isotopes. Chemical Geology, 204(3-4), pp. 201-214.
761 doi.org/10.1016/j.chemgeo.2003.11.015
762 Johnson, T.M. and Bullen, T.D. (2003). Selenium isotope fractionation during reduction by
763 Fe(II)-Fe(III) hydroxide-sulfate (green rust). Geochimica et Cosmochimica Acta, 67(3), pp.
764 413-419. doi.org/10.1016/S0016-7037(02)01137-7
765 Johnson, T.M., Herbel, M.J., Bullen, T.D. and Zawislanski, P.T. (1999). Selenium isotope
766 ratios as indicators of selenium sources and oxyanion reduction. Geochimica et
767 Cosmochimica Acta, 63(18), pp. 2775-2783. doi.org/10.1016/S0016-7037(99)00279-3
768 Kajiwara, Y., Sasaki, A. and Matsubaya, O. (1981). Kinetic Sulfur Isotope Effects in the
769 Thermal-Decomposition of Pyrite. Geochemical Journal, 15(4), pp. 193-197.
770 doi.org/10.2343/geochemj.15.193
771 Kipp, M.A., Stueken, E.E., Bekker, A. and Buick, R. (2017). Selenium isotopes record
772 extensive marine suboxia during the Great Oxidation Event. Proc Natl Acad Sci U S A,
773 114(5), pp. 875-880. doi.org/10.1073/pnas.1615867114
774 König, S., Luguet, A., Lorand, J.-P., Wombacher, F. and Lissner, M. (2012). Selenium and
775 tellurium systematics of the Earth's mantle from high precision analyses of ultra-depleted
776 orogenic peridotites. Geochimica et Cosmochimica Acta, 86, pp. 354-366.
777 doi.org/10.1016/j.gca.2012.03.014
778 König, S., Lissner, M., Lorand, J.-P., Bragagni, A., Luguet, A. (2015). Mineralogical control of

779 selenium, tellurium and highly siderophile elements in the Earth's mantle: Evidence from
780 mineral separates of ultra-depleted mantle residues. Chemical Geology. 396. pp. 16-24.
781 10.1016/j.chemgeo.2014.12.015
782 Krouse, H.R. (1977). Sulfur Isotope Studies and Their Role in Petroleum Exploration. Journal
783 of Geochemical Exploration, 7(2), pp. 189-211. doi.org/10.1016/0375-6742(77)90081-4
784 Krouse, H.R. and Thode, H.G. (1962). Thermodynamic Properties and Geochemistry of
785 Isotopic Compounds of Selenium. Canadian Journal of Chemistry, 40(2), pp. 367-375
786 doi.org/10.1139/v62-055.
787 Kurzawa, T., Konig, S., Labidi, J., Yierpan, A. and Schoenberg, R. (2017). A method for Se
788 isotope analysis of low ng-level geological samples via double spike and hydride generation
789 MC-ICP-MS. Chemical Geology, 466, pp. 219-228.
790 doi.org/10.1016/j.chemgeo.2017.06.012
791 Labidi, J., König, S., Kurzawa, T., Yierpan, A., Schoenberg, R. (2018). The selenium isotopic
792 variations in chondrites are mass-dependent; Implications for sulfide formation in the early
793 solar system. Earth and Planetary Science Letters. 481. 212-222. 10.1016/j.epsl.2017.10.032
794 Large, R.R., Halpin, J.A., Danyushevsky, L.V., Maslennikov, V.V., Bull, S.W., Long, J.A.,
795 Gregory, D.D., Lounejeva, E., Lyons, T.W., Sack, P.J., McGoldrick, P.J., Calver, C.R.
796 (2014). Trace element content of sedimentary pyrite as a new proxy for deep-time ocean–
797 atmosphere evolution. Earth Planet Sci Lett. 389, pp. 209–220
798 Layton-Matthews, D., Leybourne, M.I., Peter, J.M., Scott, S.D., Cousens, B. and Eglington,
799 B.M. (2013). Multiple sources of selenium in ancient seafloor hydrothermal systems:
800 Compositional and Se, S, and Pb isotopic evidence from volcanic-hosted and volcanic-
801 sediment-hosted massive sulfide deposits of the Finlayson Lake District, Yukon, Canada.
802 Geochimica et Cosmochimica Acta, 117, pp. 313-331. doi.org/10.1016/j.gca.2013.05.002
803 Lyons, T.W., Reinhard, C.T. and Planavsky, N.J. (2014). The rise of oxygen in Earth's early
804 ocean and atmosphere. Nature, 506(7488), pp. 307-15. doi.org/10.1038/nature13068

805 Machel, H.G., Krouse, H.R. and Sassen, R. (1995). Products and Distinguishing Criteria of
806 Bacterial and Thermochemical Sulfate Reduction. Applied Geochemistry, 10(4), pp. 373-
807 389. doi.org/10.1016/0883-2927(95)00008-8
808 Meshoulam, A., Geoffrey, S.E., Said Ahmad, W., Deev, A., Sessions, A.L., Tang, Y.,Adkins,
809 J.F., Jinzhong, L., Gilhooly III, W.P ., Aizenshata, Z., Amrani, A. (2016). Study of
810 thermochemical sulfate reduction mechanism using compound specific sulfur isotope
811 analysis. Geochimica et Cosmochimica Acta 188, 73-92.
812 Mitchell, K., Couture, R.M., Johnson, T.M., Mason, P.R.D. and Van Cappellen, P. (2013).
813 Selenium sorption and isotope fractionation: Iron(III) oxides versus iron(II) sulfides.
814 Chemical Geology, 342, pp. 21-28. doi.org/10.1016/j.chemgeo.2013.01.017
815 Mitchell, K., Mansoor, S.Z., Mason, P.R.D., Johnson, T.M. and Van Cappellen, P. (2016).
816 Geological evolution of the marine selenium cycle: Insights from the bulk shale delta Se-
817 82/76 record and isotope mass balance modeling. Earth and Planetary Science Letters, 441,
818 pp. 178-187. doi.org/10.1016/j.epsl.2016.02.030
819 Mitchell, K., Mason, P.R.D., Van Cappellen, P., Johnson, T.M., Gill, B.C., Owens, J.D., Diaz,
820 J., Ingall, E.D., Reichart, G.J. and Lyons, T.W. (2012). Selenium as paleo-oceanographic
821 proxy: A first assessment. Geochimica et Cosmochimica Acta, 89, pp. 302-317.
822 doi.org/10.1016/j.gca.2012.03.038
823 Ohmoto H. and Rye R.O. (1979) Isotopes of sulfur and carbon. In: Geochemistry of
824 Hydrothermal Ore Deposits, 2nd Edition., pp. 509 567, Wiley, New York
825 Oliver, N.H.S., Hoering, T.C., Johnson, T.W., Rumble, D. and Shanks, W.C. (1992). Sulfur
826 Isotopic Disequilibrium and Fluid-Rock Interaction during Metamorphism of Sulfidic Black
827 Shales from the Waterville-Augusta Area, Maine, USA. Geochimica et Cosmochimica Acta,
828 56(12), pp. 4257-4265. doi.org/10.1016/0016-7037(92)90266-L
829 Oremland, R.S. (1994). Biogeochemical transformations of selenium in anoxic environments.
830 W.T. Frankenberger, S. Benson (Eds.), Selenium in the Environment, Marcel Dekker, New

831 York, pp. 389-419.
832 Pogge von Strandmann, P.A.E., Coath, C.D., Catling, D.C., Poulton, S.W. and Elliott, T.
833 (2014). Analysis of mass dependent and mass independent selenium isotope variability in
834 black shales. J. Anal. At. Spectrom., 29(9), pp. 1648-1659. doi.org/10.1039/c4ja00124a
835 Pogge von Strandmann, P.A.E., Stüeken, E.E., Elliott, T., Poulton, S.W., Dehler, C.M.,
836 Canfield, D.E. and Catling, D.C. (2015). Selenium isotope evidence for progressive
837 oxidation of the Neoproterozoic biosphere. Nat. Commun., 6(10157).
838 doi.org/10.1038/ncomms10157
839 Reinhard, C.T., Planavsky, N.J. and Lyons, T.W. (2013). Long-term sedimentary recycling of
840 rare sulphur isotope anomalies. Nature, 497(7447), pp. 100-3. doi.org/10.1038/nature12021
841 Rouxel, O., Fouquet, Y. and Ludden, J.N. (2004). Subsurface processes at the Lucky Strike
842 hydrothermal field, Mid-Atlantic Ridge: Evidence from sulfur, selenium, and iron isotopes.
843 Geochimica et Cosmochimica Acta, 68(10), pp. 2295-2311.
844 doi.org/10.1016/j.gca.2003.11.029
845 Rouxel, O., Ludden, J., Carignan, J., Marin, L. and Fouquet, Y. (2002). Natural variations of Se
846 isotopic composition determined by hydride generation multiple collector inductively
847 coupled plasma mass spectrometry. Geochimica et Cosmochimica Acta, 66(18), pp. 3191-
848 3199. doi.org/10.1016/S0016-7037(02)00918-3
849 Schilling, K., Johnson, T.M. and Wilcke, W. (2011). Isotope Fractionation of Selenium During
850 Fungal Biomethylation by Alternaria alternata. Environmental Science & Technology,
851 45(7), pp. 2670-2676. doi.org/10.1021/es102926p
852 Schirmer, T., Koschinsky, A. and Bau, M. (2014). The ratio of tellurium and selenium in
853 geological material as a possible paleo-redox proxy. Chemical Geology, 376, pp. 44-51.
854 doi.org/10.1016/j.chemgeo.2014.03.005
855 Stüeken, E.E. (2017). Selenium Isotopes as a Biogeochemical Proxy in Deep Time. Reviews in
856 Mineralogy and Geochemistry, 82(1), pp. 657-682. doi.org/10.2138/rmg.2017.82.15

857 Stüeken, E.E., Buick, R. and Anbar, A.D. (2015a). Selenium isotopes support free O2 in the
858 latest Archean. Geology, 43(3), pp. 259-262. doi.org/10.1130/g36218.1
859 Stüeken, E.E., Buick, R., Bekker, A., Catling, D., Foriel, J., Guy, B.M., Kah, L.C., Machel,
860 H.G., Montanez, I.P. and Poulton, S.W. (2015b). The evolution of the global selenium
861 cycle: Secular trends in Se isotopes and abundances. Geochimica et Cosmochimica Acta,
862 162, pp. 109-125. doi.org/10.1016/j.gca.2015.04.033
863 Vollstaedt, H., Mezger, K. and Leya, I. (2016). The isotope composition of selenium in
864 chondrites constrains the depletion mechanism of volatile elements in solar system
865 materials. Earth and Planetary Science Letters, 450, pp. 372-380.
866 doi.org/10.1016/j.epsl.2016.06.052
867 Wang, Z. and Becker, H. (2014). Abundances of sulfur, selenium, tellurium, rhenium and
868 platinum-group elements in eighteen reference materials by isotope dilution Sector-field
869 ICP-MS and Negative TIMS. Geostandards and Geoanalytical Research, 38(2), pp. 189-209.
870 doi.org/10.1111/j.1751-908X.2013.00258.x
871 White, A.F., Dubrovsky, N.M. (1994). Chemical oxidation–reduction controls on selenium
872 mobility in groundwater systems. W.T. Frankenberger, S. Benson (Eds.), Selenium in the
873 Environment, Marcel Dekker, New York, pp. 185-221.
874 Wilson, S.A., Ridley, W.I. and Koenig, A.E. (2002). Development of sulfide calibration
875 standards for the laser ablation inductively-coupled plasma mass spectrometry technique.
876 Journal of Analytical Atomic Spectrometry, 17(4), pp. 406-409. doi.org/10.1039/b108787h
877 Wohlgemuth-Ueberwasser, C.C., Viljoen, F., Petersen, S. and Vorster, C. (2015). Distribution
878 and solubility limits of trace elements in hydrothermal black smoker sulfides: An in-situ
879 LA-ICP-MS study. Geochimica et Cosmochimica Acta, 159, pp. 16-41.
880 doi.org/10.1016/j.gca.2015.03.020
881 Yamamoto, M. (1984). Sulfur Isotope Effects in the Thermal Breakdown of Pyrite. Earth and
882 Planetary Science Letters, 69(2), pp. 335-340. doi.org/10.1016/0012-821x(84)90192-4

Yierpan, A., König, S., Labidi, J., Kurzawa, T., Babechuk, M.G. and Schoenberg, R. (2018). Chemical Sample Processing for Combined Selenium Isotope and Selenium–tellurium Elemental Investigation of the Earth's Igneous Reservoirs. Geochemistry, Geophysics, Geosystems. doi.org/10.1002/2017gc007299

Zack, T. and Hogmalm, K.J. (2016). Laser ablation Rb/Sr dating by online chemical separation of Rb and Sr in an oxygen-filled reaction cell. Chemical Geology, 437, pp. 120-133. doi.org/10.1016/j.chemgeo.2016.05.027

Zhu, J.-M., Johnson, T.M., Clark, S.K. and Zhu, X.-K. (2008). High Precision Measurement of Selenium Isotopic Composition by Hydride Generation Multiple Collector Inductively Coupled Plasma Mass Spectrometry with a $^{74}Se$-$^{77}Se$ Double Spike. Chinese Journal of Analytical Chemistry, 36(10), pp. 1385-1390. doi.org/10.1016/s1872-2040(08)60075-4

FIGURE LEGENDS

Fig. 1

A) Location map of Navajún, Cameros Basin, Spain. B) Specimen of Navajún pyrite used in this study. C) Back-scatter image and zones of pyrite analyzed by LA-ICP-MS.

Fig. 2

Comparison of Se and Te concentrations obtained from LA-ICP-MS (Electronic Appendix) and (isotope dilution) ID-ICP-MS (Table 1), respectively. B) $\delta^{82/76}Se_{NIST3149}$ (reported as $\delta^{82}Se$ throughout the study) vs. ng Se digested for analysis (Se concentration in $\mu g\ g^{-1}$) showing excellent reproducibility of RP samples (RP-1 to -11) of $\delta^{82}Se = -2.73 \pm 0.09$ ‰ (2 s.d.) over all Se amounts and poor reproducibility of microsamples (SPL) irrespective of the Se amount digested for analysis. Replicate analyses of unrepresentative powder (UP-1a,b and UP-2a,b) are also within themselves well reproducible but yield different absolute $\delta^{82}Se$, respectively, indicating the effect of sample heterogeneity. C) $\delta^{82}Se$ vs. Se and D) vs. Te concentration (all in $\mu g\ g^{-1}$.).

910

911 Fig. 3

912 A) $\delta^{82}Se$ vs. $\delta^{34}S$ for all SPL and RP samples where both isotopes were analyzed. Note that only
913 SPL-3 is shown here with such low $\delta^{82}Se$ = -4.40 ‰, because for SPL-8, with $\delta^{82}Se$ = -4.07 ‰, $\delta^{34}S$
914 was not obtained. Horizontal arrow indicates variable $\delta^{34}S$ due to mixing of two different $H_2S$ fluids
915 from sulfide dissolution (SD) vs. thermochemical sulfate reduction (TSR) endmembers,
916 respectively (model by Alonso-Azcárarate et al., 1999a). Horizontal arrow indicates, at relatively
917 confined $\delta^{34}S$, variable TSR-induced $\delta^{82}Se$. C) Pourbaix diagram for S (grey shaded areas) and Se
918 (black lines). TSR has an effect on both S and Se isotope fractionation. On the other hand,
919 conditions during SD remain at low Eh, therefore inhibiting strong Se isotope fractionation but a
920 allowing kinetic S isotope fractionation in response to subtle reduction following little $H_2O$-caused
921 oxidation. See text for details. B) Schematic flow chart illustrating the two fluids that scavenge S
922 and Se from their sources A and B and may explain coupled and decoupled S-Se isotope
923 fractionations in either fluid respectively. S isotope model from Alonso-Azcárarate et al., 1999a to
924 which our Se isotope data and model are fitted.

925

926 Fig. 4

927 Mixing model following the scenario of Alonso-Azcárarate et al. (1999a), where variable SD-TSR
928 mixtures are assumed to account for the entire range of $\delta^{34}S$ seen among Navajún pyrites within the
929 Cameros Basin and at the microscale within single pyrite specimens. Following the observation that
930 $\delta^{82}Se$ are decoupled from $\delta^{34}S$ with almost complementary trends (see Fig. 3a), the co-evolution of
931 both signatures can be modeled (dotted lines). For S we use the most positive and negative $\delta^{34}S$
932 values in our pyrite microsamples as captured TSR and SD endmembers, repectively ($\delta^{34}S$ = -4.7
933 and -8 ‰) and most negative and positive $\delta^{82}Se$ values of our analyzed microsamples as TSR and
934 SD endmembers, respectively ($\delta^{82}Se$ = -4.4 and -0.4 ‰). S/Se ratio of fluid from source A needs to
935 be higher than fluid S/Se from source B by at least factor 20 but may range up to 200. A This agrees

936 with a 20 to 200-fold higher S/Se ratio in gypsum compared to sulfide. See text and Electronic
937 Appendix for further details.
938
939 Fig. 5
940 Potential of combined S-Se isotopes in single sulfides for palaeo-redox studies. A) Terrestrial
941 evolution of $O_2$ through geological time in billion years (Gyr) after Lyons et al. (2014) with fine-
942 black, stippled line for the estimated oxygenation curve based on the Se content of sedimentary
943 pyrite (after Large et al., 2014). Numbers depict potential scenarios where S-Se decoupling may
944 occur across critical time periods in Earth's geological history, such as potential pre-GOE whiffs of
945 oxygen (Anbar et al., 2007) or the second significant atmospheric oxygen increase to the present
946 atmospheric level (PAL) in the Neoproterozoic. B) Large redox variation (1), where an upper
947 minimum is suggested by subsequent or simultaneous S and Se isotope excursions C). D) Restricted
948 redox variation (2), where an upper maximum is likely due to lack of Se isotope at simultaneously
949 strong S isotope variations. E) Restricted redox variation (3), where a lower limit on oxygen drop is
950 suggested by significant Se isotope but no S isotope variations. Note that the scenarios presented
951 here are only for combined S-Se signatures in single sulfides, where bias from individual excursions
952 of either system or mixing of various minerals are not relevant. For instance S isotope excursions
953 alone may occur even before the GOE to some extent due to bacterial reduction of atmospherically
954 generated sulfate. Lines and grey shading in b, c, d as in Fig. 3c.
955

**Table**

**Table 1.** Sulfur-Selenium isotope and S-Se-Te concentration data obtained in this study (Solution data only, all LA-ICP-MS data are reported in the Eletronic Appendix)

| Sample | mg digested | Se (µg g $^{-1}$) | $\delta^{82}$Se (‰) | S (wt.%) | $\delta^{34}$S (‰) | Te (µg g $^{-1}$) |
|---|---|---|---|---|---|---|
| RP-1 | 20.1 | 5.04 | -2.66 | 51.5 | -5.3 | 0.264 |
| RP-2 | 29.3 | 5.05 | -2.73 | 49.9 | -5.3 | 0.258 |
| RP-3 | 39.5 | 5.04 | -2.70 | 50.4 | -5.4 | 0.266 |
| RP-4 | 49.9 | 5.14 | -2.76 | - | - | - |
| RP-5 | 52.8 | 5.15 | -2.77 | - | - | - |
| RP-6 | 55.9 | 5.14 | -2.67 | - | - | - |
| RP-7 | 50.4 | 5.15 | -2.76 | - | - | - |
| RP-8 | 51.4 | 5.06 | -2.72 | - | - | 0.262 |
| RP-9 | 53.4 | 5.12 | -2.70 | - | - | 0.266 |
| RP-10 | 5.51 | 4.87 | -2.79 | - | - | - |
| RP-11 | 12.2 | 5.01 | -2.75 | - | - | - |
| | | | | | | |
| UP-1a | 50.3 | 4.40 | -2.13 | - | - | - |
| UP-1b | 51.2 | 4.46 | -2.15 | - | - | - |
| UP-2a | 50.9 | 4.97 | -1.31 | - | - | - |
| UP-2b | 51.4 | 4.94 | -1.30 | - | - | - |
| | | | | | | |
| SPL-1 | 3.67 | 4.26 | -0.43 | 49.9 | -6.3 | 0.378 |
| SPL-2 | 4.75 | 5.76 | -1.56 | 53.3 | -4.5 | 0.182 |
| SPL-3 | 5.03 | 5.71 | -4.40 | 47.3 | -5.3 | 0.210 |
| SPL-4 | 10.2 | 6.55 | -2.13 | 40.4 | -4.4 | 0.243 |
| SPL-5 | 9.96 | 6.55 | -0.39 | 50.5 | -7.1 | 0.243 |
| SPL-6 | 12.8 | 4.75 | -0.41 | 57.1 | -6.6 | 0.370 |
| SPL-7 | 12.2 | 4.71 | -0.83 | 52.3 | -4.7 | 0.304 |
| SPL-8 | 3.48 | 4.74 | -4.07 | - | - | 0.235 |
| SPL-9 | 7.02 | 3.61 | -0.71 | - | - | 0.216 |
| SPL-10 | 5.02 | 3.58 | -0.45 | - | - | 0.288 |
| BHVO-2* | 299 | 0.168 | 0.14 | - | - | 0.0142 |

All $\delta^{82/76}Se_{NIST3149}$ are reported as $\delta^{82}$Se. Internal errors (2 s.e.) below 0.1‰. Average $\delta^{82}$Se of RP-1 to 11 = -2.73 ± 0.09‰ (2 s.d.). BHVO-2* analyzed together with RP samples and published by Yierpan et al. (2018) as part of a study assessing long-term BHVO-2 reproducibility, which is $\delta^{82}$Se = 0.18 ± 0.10‰ (2 s.d., n=8, multiple analytical sessions over 6 months). All $\delta^{34}$S data are normalized to Vienna Canyon Diablo Troilite (V-CDT) and subject to a long-term reproducibility of ±0.3‰ (2 s.d.).

**Figure**

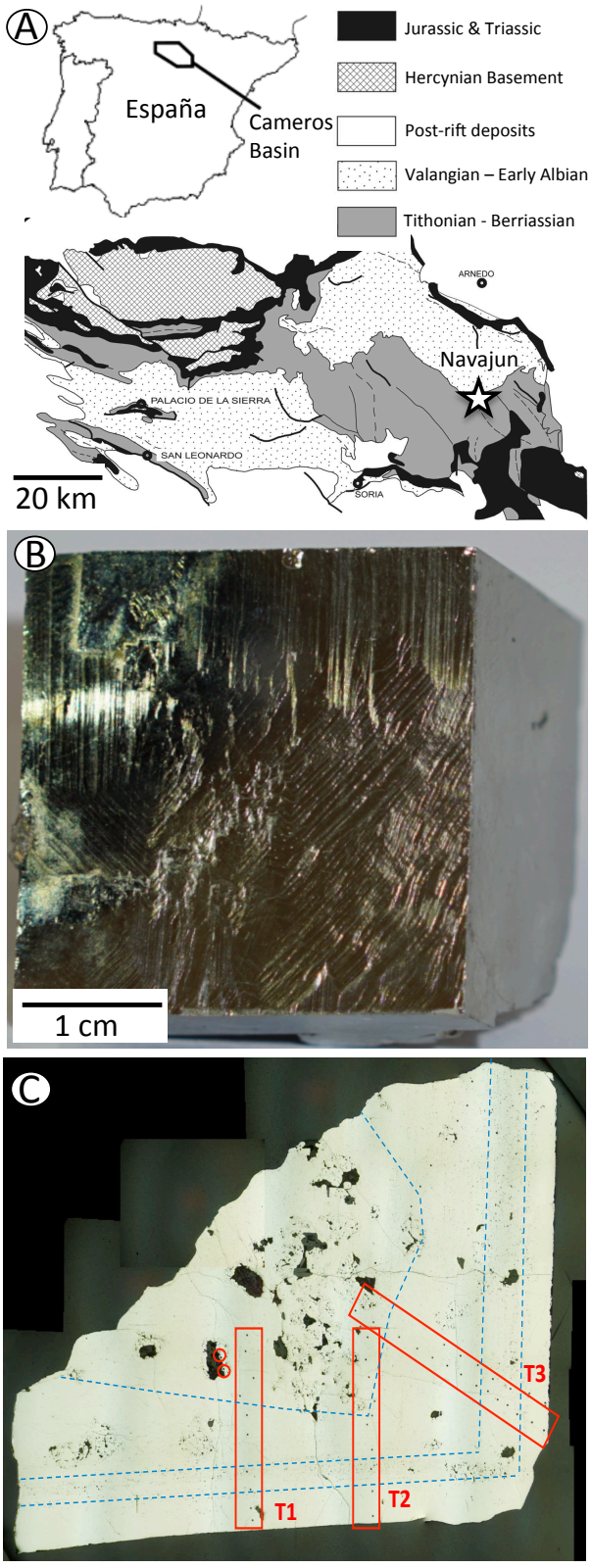


Figure 1
König et al.

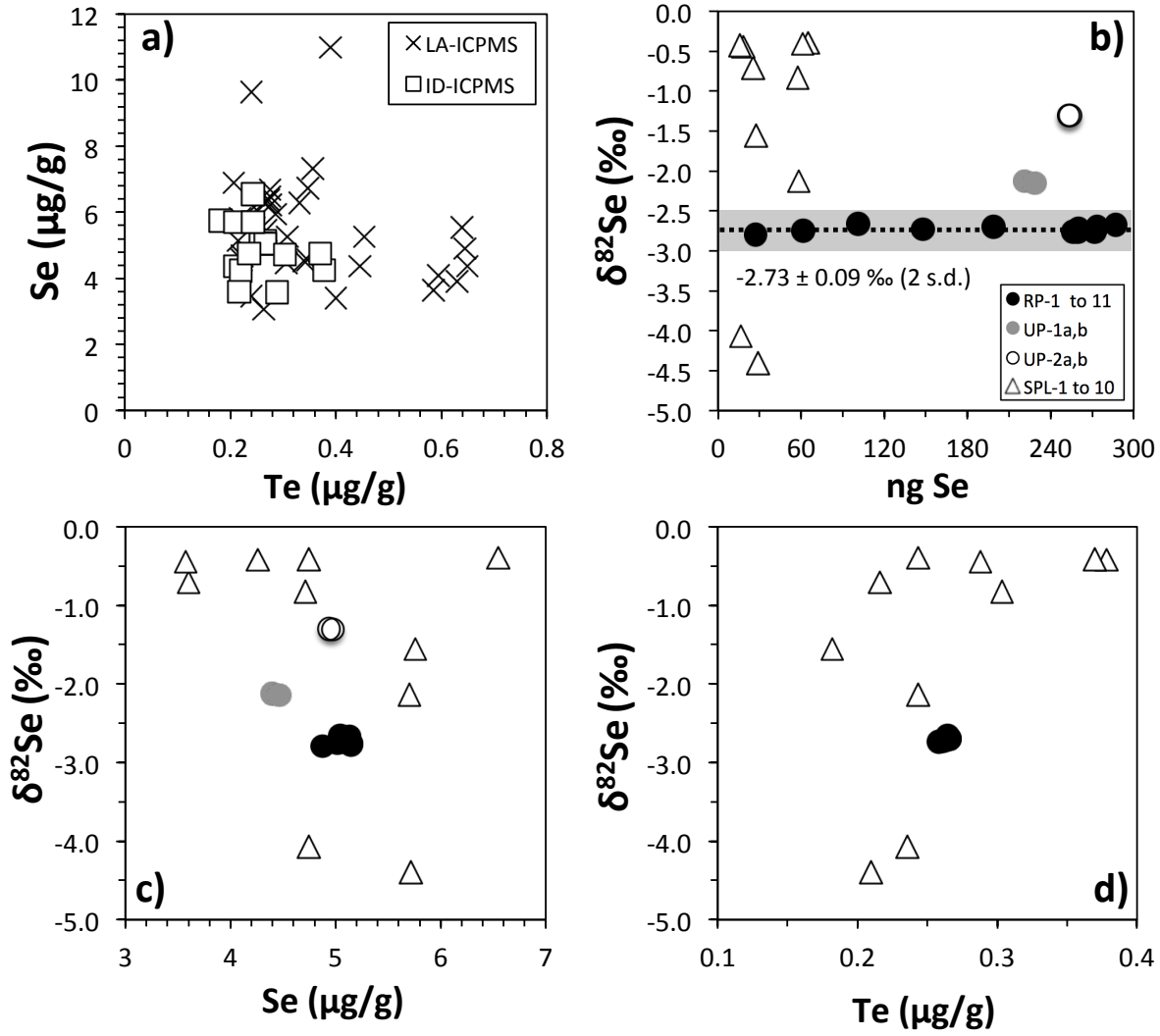


Figure 2
König et al.

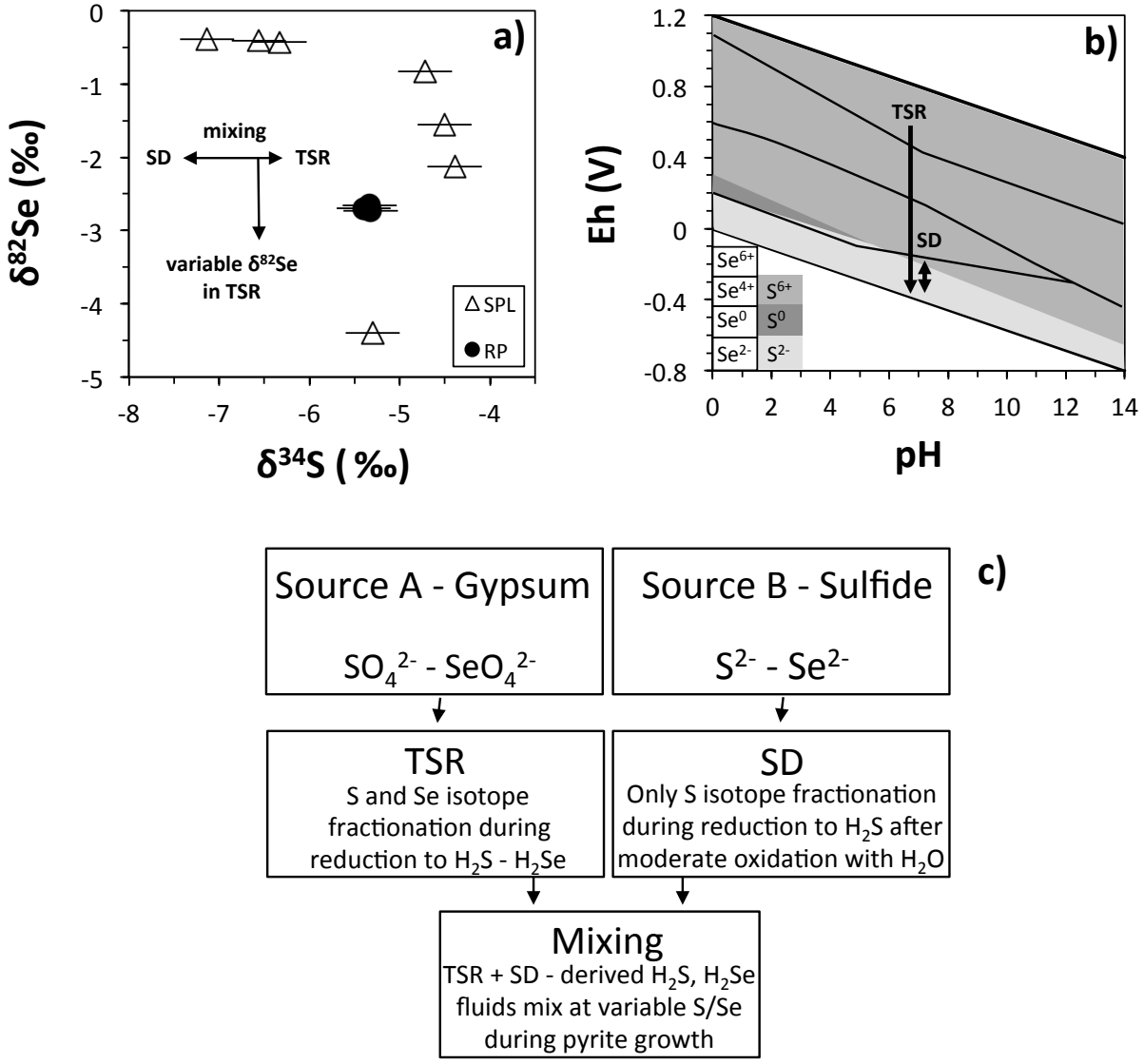


Figure 3
König et al.

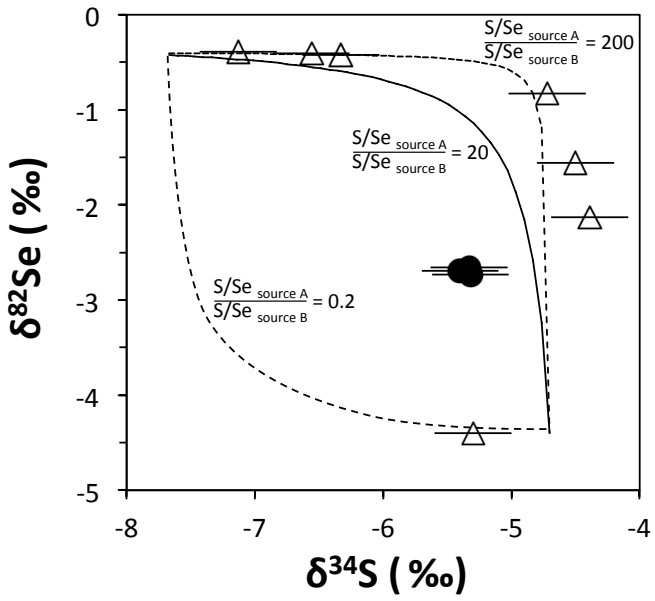


Figure 4
König et al.

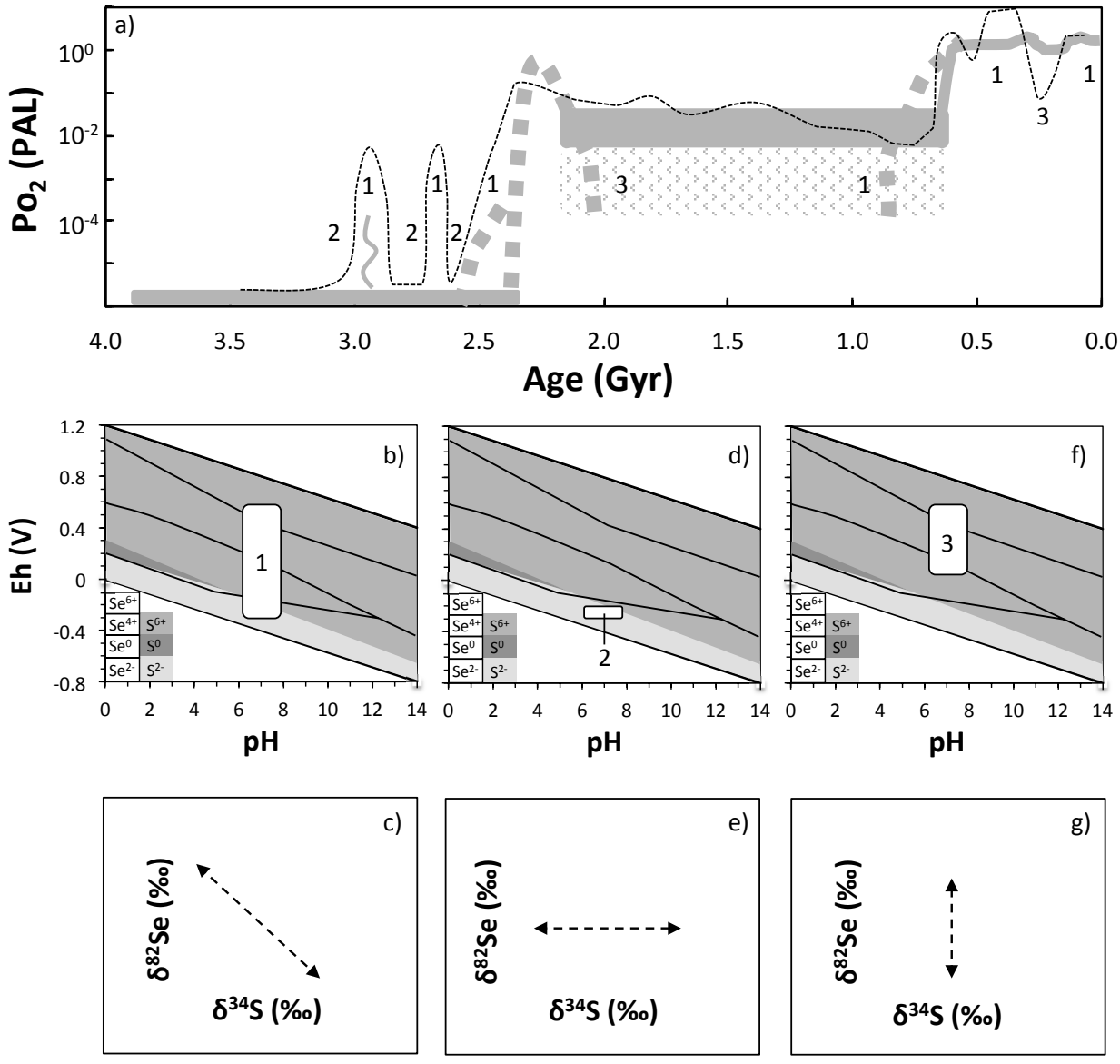


Figure 5
König et al.